Transport, diffusion, and energy studies in the Arnold-Beltrami-Childress map

Swetamber Das* and Neelima Gupte†

Department of Physics, Indian Institute of Technology Madras, Chennai, 600036, India

(Received 27 March 2017; published 11 September 2017)

We study the transport and diffusion properties of passive inertial particles described by a six-dimensional dissipative bailout embedding map. The base map chosen for the study is the three-dimensional incompressible Arnold-Beltrami-Childress (ABC) map chosen as a representation of volume preserving flows. There are two distinct cases: the two-action and the one-action cases, depending on whether two or one of the parameters (A,B,C) exceed 1. The embedded map dynamics is governed by two parameters (α,γ), which quantify the mass density ratio and dissipation, respectively. There are important differences between the aerosol ($\alpha < 1$) and the bubble ($\alpha > 1$) regimes. We have studied the diffusive behavior of the system and constructed the phase diagram in the parameter space by computing the diffusion exponents η. Three classes have been broadly classified—subdiffusive transport ($\eta < 1$), normal diffusion ($\eta \approx 1$), and superdiffusion ($\eta > 1$) with $\eta \approx 2$ referred to as the ballistic regime. Correlating the diffusive phase diagram with the phase diagram for dynamical regimes seen earlier, we find that the hyperchaotic bubble regime is largely correlated with normal and superdiffusive behavior. In contrast, in the aerosol regime, ballistic superdiffusion is seen in regions that largely show periodic dynamical behaviors, whereas subdiffusive behavior is seen in both periodic and chaotic regimes. The probability distributions of the diffusion exponents show power-law scaling for both aerosol and bubbles in the superdiffusive regimes. We further study the Poincáre recurrence times statistics of the system. Here, we find that recurrence time distributions show power law regimes due to the existence of partial barriers to transport in the phase space. Moreover, the plot of average particle kinetic energies versus the mass density ratio for the two-action case exhibits a devil's staircase–like structure for higher dissipation values. We explain these results and discuss their implications for realistic systems.

DOI: 10.1103/PhysRevE.96.032210

I. INTRODUCTION

The study of transport and diffusion of impurities in fluid flow has significant practical implications for diverse areas of science. Examples include the dynamics of passive scalars in fluid models [1–5], atmospheric motion [6,7], flows in planetary science [8], and in several engineering applications [9,10]. A number of studies of the chaotic advection of finite-size passive and active particles in fluids exist ([11–21]) (see Ref. [22] for the most recent review on chaotic advection).

However, most of these studies consider two-dimensional (2D), and quasi-two-dimensional models. The dynamics of impurities in models of three-dimensional (3D) fluids has received relatively limited attention [23–27] despite their obvious implications for practical applications. Such impurities can be effectively modelled by the bailout embedding maps of 3D volume preserving maps [15]. The dynamical behavior of these systems has been studied elsewhere [28]. Here, we consider the dynamical and statistical properties of impurity transport in 3D incompressible flows by investigating such embedding maps.

The Lagrangian dynamics of small spherical tracers in nonuniform, incompressible flows is described by the Maxey-Riley (MR) equations [29], under the assumption of local incompressibility. The MR equation, under various approximations [27], leads to a set of minimal equations for neutrally buoyant tracers, known as the embedding equations [14,27]. In the case of nonneutrally buoyant tracers for which the particle density differs from the surrounding fluid density, the embedding equations lead to a generalized set of discretized equations [30]. Such map analogues of the embedding equations preserve the features of the embedding dynamics under which the fluid dynamics is embedded in the particle dynamics and may be recovered under appropriate limits. The particle motion in the flow thus becomes dissipative in nature and gives rise to regions of contraction and expansion without affecting the incompressible nature of the Lagrangian fluid flow. The underlying idea of the generalized embedding is that the difference in the densities of the fluid and the particles results in their trajectories separating from each other. This has interesting consequences for diffusion and transport properties of the system [31–35].

Bail-out embeddings of two- and three-dimensional flows, as well as maps have been studied earlier [15,18,19,28]. In the two-dimensional case, wherein the base fluid flow was modelled by an area-preserving map, the standard map, the predominant dynamical regimes in the system are the periodic regime, the chaotic structure regime, and the mixing regime. The nature of the inertial particles whether heavier (aerosol) or lighter (bubble) than the base flow, in the three dynamical regimes, was shown to have definite consequences for the diffusion, drift, and recurrence properties of the system [18,19]. Chaotic structure regimes contained inhomogeneous sticky regimes in the phase space, and these contributed power-law tails to the recurrence time distributions and jump length distributions. Superdiffusive behavior was observed for the periodic regimes of both types of passive scalars. The dynamical and transport phase diagrams of the systems showed distinctly correlated behavior [19].

*swetdas@physics.iitm.ac.in
†gupte@physics.iitm.ac.in

Our recent study of the bail-out embeddings of three-dimensional volume-preserving maps [28] identified a set of rich structures with complex dynamics. Here, the motion of the advected particles is represented in the Lagrangian description by an embedding map with the volume preserving Arnold-Beltrami-Childress (ABC) map as the base map. The resulting embedded ABC map is invertible and dissipative involving two sets of parameters, namely (A,B,C), which belong to the base map, and the mass ratio and dissipation parameters, (α,γ) due to the embedding method, which is described in next section. We considered one and two-action versions of the ABC map. Three types of dynamical behaviors—periodic orbits, chaotic and hyperchaotic regions were found to be present. The bubble regime in the two-action case was seen to be mostly hyperchaotic, but the corresponding aerosol regime also contained a tongue of hyperchaoticity at low values of dissipation. Crisis-induced intermittency was seen in this region, and power-law behavior for the characteristic times between bursts along with unstable dimension variability was observed in the neighborhood of the crisis. The bubble regime also displayed the existence of multiple coexisting attractors and a riddled basin of attraction with several windows of interior crisis. An interesting two-ring attractor was observed in the post crisis setting with trajectories hopping between the rings with period two. We had also carried out a preliminary study for the one-action case of the ABC map, wherein the aerosol regime with $\alpha = 0.2$ where the largest Lyapunov exponent was seen to be negative for most of the range $0 \leqslant \gamma \leqslant 4$, and periodic attractors with even periods were seen. The bubble regime with $\alpha = 1.25$ showed fully hyperchaotic behavior and patched structures appeared in the phase-space plots in some cases. Thus, our toy model showed a variety of phenomena that could lead to consequences for transport and pattern formation. In this paper, we explore the diffusion and transport properties of the embedded ABC map. We use Lyapunov exponent analysis, diffusion studies, and recurrence time statistics to investigate the clustering and concentration phenomena seen here. Similar studies have been carried out for the 2D area preserving case earlier [18,19]. We expect that the presence of a third dimension in the underlying flow will contribute its own signatures to the clustering and transport properties seen here.

We note that the bailout embeddings of the ABC maps have also been studied in Refs. [15,16] for the case where the impurities are neutrally buoyant. It has been shown that the neutrally buoyant impurities detach themselves from the fluid trajectories near hyperbolic lines and tend to accumulate in the tubular regions of the phase space of the ABC map. This results in the formation of 3D structures in the phase space. Furthermore, particle dynamics with noise was also studied in these references, wherein a temperature amplitude is defined that connects the variances of the separation between fluid and particle velocities and noise at a given point in the phase space. The results show that the particles appear to avoid the points with larger values of the amplitude and prefers those with smaller values. In contrast, our study discusses the transport of impurities of the aerosols and bubbles types in the ABC flow. However, we have not considered the effects of noise in this paper.

This paper is organized as follows. Section II outlines the theoretical formulation of the embedded map model. The dynamical regimes and the phase diagram based on the Lyapunov exponents of the one-action case have been discussed in Sec. III. The study of recurrence time statistics and the diffusion properties of the system have been described in Secs. V and IV, respectively. Energy studies for the impurity particles in the embedded map are discussed in Sec. VII. The major findings of the paper are then summarized together with a discussion of their implications in Sec. VIII. The Appendix gives a short derivation of the bailout embedding map from the Maxey-Riley equations.

II. THE BAILOUT EMBEDDING MAP: DYNAMICAL REGIMES AND PHASE DIAGRAM

The transport of passive particle tracers of finite size in fluids is given by the Maxey-Riley equation [29]. Under certain simplifying assumptions (see the Appendix for details), i.e., low Reynolds number, negligible buoyancy effects, and retaining only the Bernoulli, Stokes drag, and Taylor added terms, the Maxey-Riley equation reduces to the following bailout embedding equation [15,16,28]:

$$\frac{d\mathbf{v}}{dt} - \alpha\frac{d\mathbf{u}}{dt} = -\gamma(\mathbf{v} - \mathbf{u}). \tag{1}$$

Here, the velocity of the particle and the fluid flow are given by $\mathbf{v}$ and $\mathbf{u}$, respectively, and γ is the dissipation parameter. The parameter α is the mass density ratio, $\alpha = \frac{\rho_f}{\rho_f + 2\rho_p}$, corresponding to the aerosol case ($\alpha < 1$), the bubble case ($\alpha > 1$), and the neutrally buoyant cases ($\alpha = 1$), where ρ_f and ρ_p are fluid and particle densities, respectively.

A bailout embedded version for neutrally buoyant particles where the densities of the particle and fluid are the same has been discussed for maps and flows in Refs. [14–16] and as mentioned in the Introduction. Here, the general bailout embedding for a given map $x_{n+1} = T(x_n)$ was considered to be

$$x_{n+2} - T(x_{n+1}) = K(x_n)[x_{n+1} - T(x_n)], \tag{2}$$

where the bailout function $K(x)$ is given by

$$K(x) = e^{-\gamma}\nabla T, \tag{3}$$

and γ is the dissipation parameter. In the present paper, we take into account the differences in the densities of impurity particles and the fluid, as aerosols and bubbles, described by the value of parameter α in Eq. (6). The mass density ratio α gives the aerosol case ($\alpha < 1$), the bubble case ($\alpha > 1$), and the neutrally buoyant cases ($\alpha = 1$), as stated earlier.

The bailout embedding map of Eq. (2) can also be expressed in the form [28,30]

$$\begin{aligned} x_{n+1} &= T(x_n) + \delta_n, \\ \delta_{n+1} &= e^{-\gamma}[\alpha x_{n+1} - T(x_n)]. \end{aligned} \tag{4}$$

Here, the base map $T(x_n)$ is the base map taken to be a volume-preserving map as a representation of the incompressible fluid acting as the base flow. The vector x represents the position of the particle and the vector δ defines the detachment of the particle from the fluid velocities.

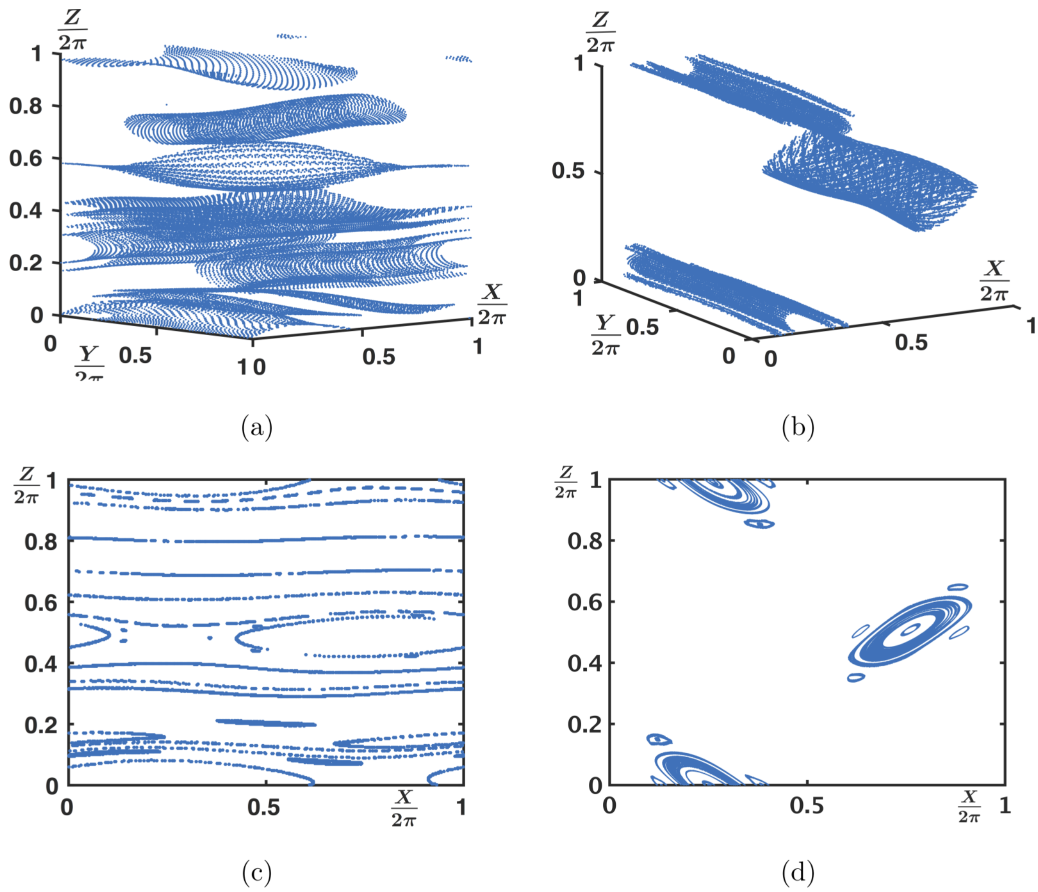

FIG. 1. (a) The configuration space of the one-action ABC map for $(A,B,C) = (1.5,0.08,0.16)$ and (b) the configuration space of the two-action ABC map for $(A,B,C) = (2,1.5,0.08)$. We only indicate regular trajectories. The configuration space of the two-action does not have any invariant sheets leading to the global transport of trajectories. The plots in (c) and (d) show the $Y = 0.5$ plane in the one and the two-action cases, respectively. In (c), the elliptic orbits indicate the existence of tubes and invariant surfaces are reflected in the form of lines spanning $\frac{X}{2\pi} = 0$ to 1. These surfaces cover the Y plane dividing the phase space in many isolated partitions. The configuration space of the two-action in (d) does not have any invariant sheets leading to global transport of trajectories. We show trajectories for 25 initial conditions randomly chosen from the uniform distribution of angles in the interval $[0,2\pi]$. The thickness of the Y plane used here is 0.01.

The dissipation parameter γ is a measure of contraction or expansion in the phase space of the particle's dynamics. The particle is said to have bailed out of the fluid trajectory when $\delta \neq 0$, where the new variable δ is defined to be the detachment of the particle from the local fluid parcel velocity [30]. The fluid dynamics is recovered under the limits $\delta \to 0$, $\alpha = 1$, and $\gamma \to \infty$. This is the sense in which the fluid dynamics is said to be embedded in the particle equations. This map is dissipative with a phase-space contraction rate $e^{-3\gamma}$. We will use this version of the bail-out embedding map in all subsequent analysis.

We use a well-known volume preserving map, the Arnold-Beltrami-Childress (ABC) map as the base map for the fluid in our work. The presence of chaotic streamlines seen in the nonintegrable case motivates its study as a prototype fluid dynamical model in three dimensions. The version of the ABC map employed here [23,36] is given by

$$\left.\begin{aligned} x_{n+1} &= x_n + A\sin(z_n) + C\cos(y_n) \\ y_{n+1} &= y_n + B\sin(x_{n+1}) + A\cos(z_n) \\ z_{n+1} &= z_n + C\sin(y_{n+1}) + B\cos(x_{n+1}) \end{aligned}\right\} \mod 2\pi. \tag{5}$$

The corresponding bailout embedded version of the ABC map is given by the following six-dimensional map [28,37]:

$$\left.\begin{aligned} x_{n+1} &= x_n + A\sin(z_n) + C\cos(y_n) + \delta_n^x \\ y_{n+1} &= y_n + B\sin(x_{n+1}) + A\cos(z_n) + \delta_n^y \\ z_{n+1} &= z_n + C\sin(y_{n+1}) + B\cos(x_{n+1}) + \delta_n^z \\ \delta_{n+1}^x &= e^{-\gamma}\big[\alpha x_{n+1} - \big(x_{n+1} - \delta_n^x\big)\big] \\ \delta_{n+1}^y &= e^{-\gamma}\big[\alpha y_{n+1} - \big(y_{n+1} - \delta_n^y\big)\big] \\ \delta_{n+1}^z &= e^{-\gamma}\big[\alpha z_{n+1} - \big(z_{n+1} - \delta_n^z\big)\big] \end{aligned}\right\} \mod 2\pi. \tag{6}$$

The ABC map and its embedded versions are implemented with modulo 2π, including the mass ratio α and dissipative parameter γ in addition to a set of real parameters (A,B,C). We investigate two quasiintegrable cases of the ABC map [23]. We will refer to the map as the one-action map if one of the parameters exceeds 1; and as the two-action version if two of parameters (A,B,C) are larger than 1. The one-action ABC map displays KAM-like invariant surfaces called resonance sheets which divides the configuration space into many isolated partitions. Figure 1(a) shows the Y plane of the one-action ABC map at $(A,B,C) = (1.5,0.08,0.16)$. The elliptic orbits indicate the existence of tubes, and resonance sheets are reflected in the form of lines spanning the range where $\frac{X}{2\pi} \in [0,1]$. These KAM barriers cover the Y plane dividing the phase space into many isolated partitions. The trajectories within these partitions remain bounded and parts of these barrier sheets break down under small perturbations, but the trajectories remain bounded within the invariant surfaces that are intact. In the two-action ABC map, on the other hand, unbounded diffusive motion occurs through the KAM barriers which are absent in the configuration space. Figure 1(b) shows the orbits on the Y plane for $(A,B,C) = (2,1.5,0.08)$, indicating the existence of tubes but the KAM barriers of resonance sheets are now absent. The resulting motion is thus unbounded and leads to the global transport of trajectories—a phenomenon known as resonance-induced diffusion. This kind of diffusion is similar to Arnold diffusion and, therefore, has significant implications for the mixing and transport properties of passive scalars.

The dynamical regimes and phase diagram for the two-action case embedded map has been described in detail earlier [28], along with a preliminary study of these regimes for the one-action case. The aerosol and bubble regimes showed remarkably different behavior. In the case of 2D flows, it was believed that for the motion of inertial particles, the elliptical islands and their neighborhoods act as centrifuges by pushing away the heavy aerosol and trapping the lighter bubbles [38,39]. However, at high values of dissipation γ, it was seen that the dissipation can counteract the influence of centrifugal force on the aerosols and trap them in the neighborhood of the islands [18]. Such trapping of aerosols has also been reported earlier for 2D open chaotic flows [40–42]. Bubbles, on the other hand, are expelled out of the invariant regions owing to the centrifugal forces but tend to be trapped in the vicinity of regular orbits at higher dissipation values. However, at small values of dissipation, bubbles may penetrate the regions of high shear through leaky barriers in the phase space [28]. Therefore, it was observed that the dynamical behavior of aerosol and bubbles sensitively depends upon both the mass density ratio α and the dissipation parameter γ.

We now discuss the dynamical regimes seen for the embedded dynamics for the one-action case of the base ABC map, followed by diffusion and transport studies for this case in the subsequent section.

III. DYNAMICAL REGIMES FOR THE ONE-ACTION CASE

The set of parameter values for (A,B,C) chosen for the one-action case under study are $(1.5,0.08,0.16)$. Our analysis of the system in the aerosol regime at $\alpha = 0.2$ showed periodic structures, whereas in the bubble regime at $\alpha = 1.2$, we found hyperchaotic behavior. If the largest two Lyapunov exponents (LEs) are indicated by λ_1 and λ_2, then a scheme to distinguish the dynamical behaviors is the following:

$$
\begin{aligned}
(\lambda_1,\lambda_2) < 0 &\Rightarrow \text{Regular/Periodic,}\\
\lambda_1 > 0, \lambda_2 < 0 &\Rightarrow \text{Chaotic,}\\
(\lambda_1,\lambda_2) > 0 &\Rightarrow \text{Hyperchaotic behaviors.}
\end{aligned}
$$

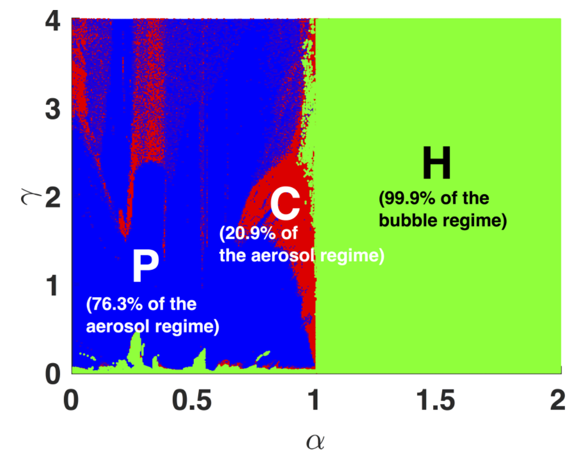

FIG. 2. The phase diagram of the embedded one-action ABC map for parameter values $(A,B,C) = (1.5,0.08,0.16)$ [periodic orbits, blue (P); chaotic behavior, red (C); hyperchaotic regions, green (H)]. The α-γ space is covered by a 400×800 mesh, each element is of size 0.005×0.005. The phase diagram has been plotted using LE-s calculated for 25 000 iterates after discarding the first 5000 iterates as transients.

Figure 2 shows the complete phase diagram using the above scheme. We have computed the two largest LEs, (λ_1,λ_2) for 25 000 iterates, discarding 5000 iterates as transients. The computations have been performed for the α-γ parameter space on a 400×800 mesh of cell size 0.005. The bubble regime ($\alpha > 1$) is predominantly hyperchaotic indicated by the color green and is labeled by "H." The aerosol regime ($\alpha < 1$), on the other hand, is covered with periodic structures (in blue and labeled by "P") and chaotic behavior (in red and labeled by "C"). The chaotic region has a tonguelike structure on the aerosol side of a reasonably sharp boundary at $\alpha = 1$ with $\gamma < 2$. In comparison with the phase diagram for the embedded two-action case (see Ref. [28]), the aerosol regime in Fig. 2 has chaotic and periodic regions, with chaotic regions with diffuse boundaries in the approximate range where $\alpha < 0.25$ and $\gamma > 1.2$. For $\gamma < 0.5$, we observe fingers of hyperchaotic regions containing a thin boundary of chaotic behavior in red. However, the bubble regimes for both the cases are almost completely hyperchaotic, indicating two diverging directions which may result in a higher efficiency of mixing and transport in the fluid flow. We note that the phase diagram is plotted after a very long asymptote, and other kinds of behavior are seen in the bubble regime in the transient.

Although the hyperchaotic regime looks simple, the phase space in these regimes has complex structures in the phase space. Deep inside the regime, for $\gamma > 3$, an interesting attractor appears which has two parts. Trajectories are seen to hop between the two parts in discrete steps. An example is shown in Fig. 3 at $(\alpha,\gamma) = (1.85,3.20)$. The attractor in Fig. 3(a) has two parts with spiralling tubular structures. The trajectory returns to each part after spending a finite amount of time in the other one. We refer to this time as the return time. Surprisingly, despite the hyper chaotic nature, i.e., $(\lambda_1,\lambda_2) > 0$, the distribution of return times to each of the parts are discrete. In Fig. 3(b), the bars in black correspond to returns to the part R of attractor for which $\frac{Y}{2\pi} < 0.5$ and those

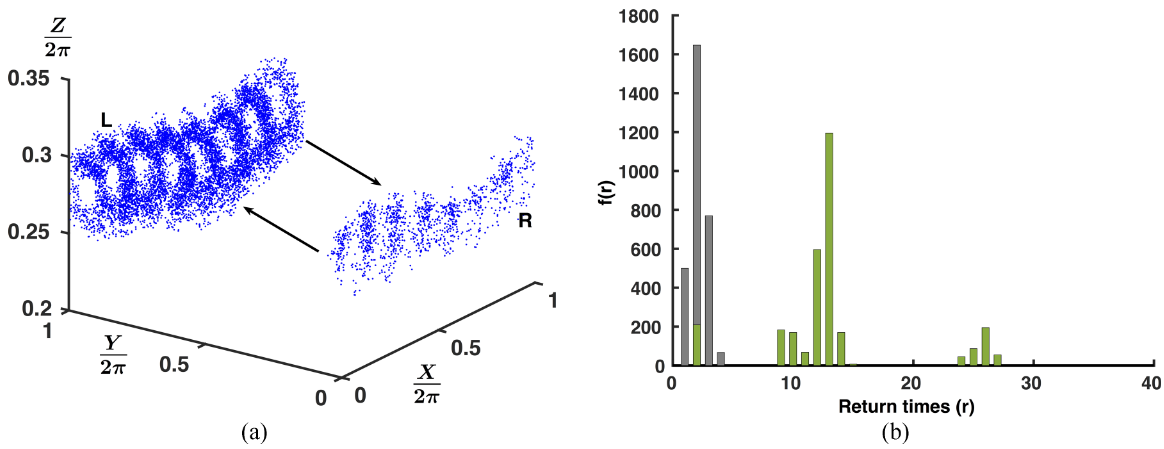

FIG. 3. (a) The attractor in the X-Y-Z configuration space of the embedded one-action map at $\alpha = 1.85$ and $\gamma = 3.2$. (b) The frequencies of return times for discrete hopping between the two parts of the attractor. The bars in black correspond to the part R for which $\frac{Y}{2\pi} < 0.5$ and those in green to the part L for which $\frac{Y}{2\pi} > 0.5$. The return times for the part R are (1,2,3,4), whereas that for the part L are (2,9,10,11,...,15,24,...,27,39). The computations are carried out for 50 000 iterates of which 5000 were discarded as transients.

in green correspond to the return to part L of the attractor for which $\frac{Y}{2\pi} > 0.5$. The computations are carried out for 50 000 iterates of which 5000 were discarded as transients. The return times for the part R are (1,2,3,4) whereas that for the part L are (2,9,10,11,...,15,24,...,27,39). We note that for the two-action case $(A,B,C) = (2.0,1.3,0.16)$, a similar attractor was seen [28] with a double ring structure at the parameter values $(\alpha,\gamma) = (0.7,2.82)$ for which the asymptotic trajectory continuously hopped between the rings with period 2. Therefore, it appears that such attractors are generic to the bubble regime in the embedded ABC map.

We now examine the transport properties using detailed diffusion studies and correlate them with the recurrence times statistics and the dynamical regimes.

IV. DIFFUSION

The transport of passive scalars in flows can be described statistically by examining the dispersion as a function of the parameters (α,γ). We consider an ensemble of N particles distributed uniformly in phase space and evolve it in time. The individual particles in the particle cloud disperse with time in the three-dimensional configurational space from their initial positions in the cloud. The dispersion of these particles is given by the variance of the displacement of particles σ^2,

$$\sigma^2(t) = \langle(\mathbf{x}(t) - \langle\mathbf{x}(t)\rangle)^2\rangle \sim Dt^\eta. \quad (7)$$

Here, $\mathbf{x}(t)$ denotes the position of a particle and $\langle\mathbf{x}(t)\rangle$ indicates the average position of all the particles at time t, both in configuration space. The diffusion coefficient D and the exponent η quantify the type of diffusion. The angular brackets denote the ensemble average. The configuration space in three dimensions considered here is the cover space, i.e., without the periodic boundary conditions which have been used later in Sec. V.

Generally, depending on the value of the exponent η in Eq. (7), the diffusion process broadly belongs to one of the three classes—subdiffusive transport ($\eta < 1$) indicates slow diffusion of particles with time, normal diffusion ($\eta \approx 1$) stands for normal transport in which the variance grows linearly with time, and superdiffusion ($\eta > 1$) implies that the trajectories of the particles have long displacements. Subdiffusive behavior in the embedding map may be further subcategorized viz., one associated with the trapping regions with stationary states while the other with trapping regions with nonstationary states. The ballistic regime where $\eta \approx 2$ is a special subset of the superdiffusive regime. We analyze the behavior of these classes below in detail, for both one-action and two-action cases and highlight the differences in their behavior.

The phase diagram of Figs. 6 and 8 maps out the distinct dynamical regimes in the (α,γ) parameter space. It will be useful to obtain a similar phase diagram that classifies the main diffusion regimes as a function of the parameters (α,γ). The value of the exponent η can be used for such a classification. For this, the log-log plot of the variance as a function of time is fitted to a straight line after discarding initial transients. We used a linear square fit for finding the value of η for each data point in the (α,γ) space.

In principle, the normal diffusion regimes in the phase diagram can be distinguished from the anomalous diffusion regimes if the values of the exponent are either $\eta < 1$ and $\eta > 1$. For instance, in Fig. 4, we show the cases of ballistic diffusion, normal diffusion, and subdiffusion. In Fig. 4(a), the system $(\alpha,\gamma) = (0.5,3.7)$ demonstrates ballistic diffusion, whereas Fig. 4(b) indicates a case of normal diffusion for $(\alpha,\gamma) = (1.21,1.45)$. For the subdiffusive regime, we identify two kinds of states—stationary and nonstationary in Figs. 4(c) and 4(d) for $(\alpha,\gamma) = (0.33,1.17)$ and $(\alpha,\gamma) = (1.21,2.75)$, respectively. The stationary states are identified when $\eta < 0.92$ when the fluctuations in $\sigma^2(t)$ during the last 2000 iterations are below 1%. The nonstationary states are near periodic states as in Fig. 4(c) for which $\eta < 0.92$ and fluctuations are above 1%. We adopt this strategy to obtain the phase diagram based on the diffusion exponent for the subdiffusive regime. As examples, we show the cover phase spaces of the two states in Figs. 5(a) and 5(b)—stationary and nonstationary states, respectively, for the same set of (α,γ) values as in Figs. 4(c) and 4(d). For computations, we consider 2×10^4 iterations with 10^3

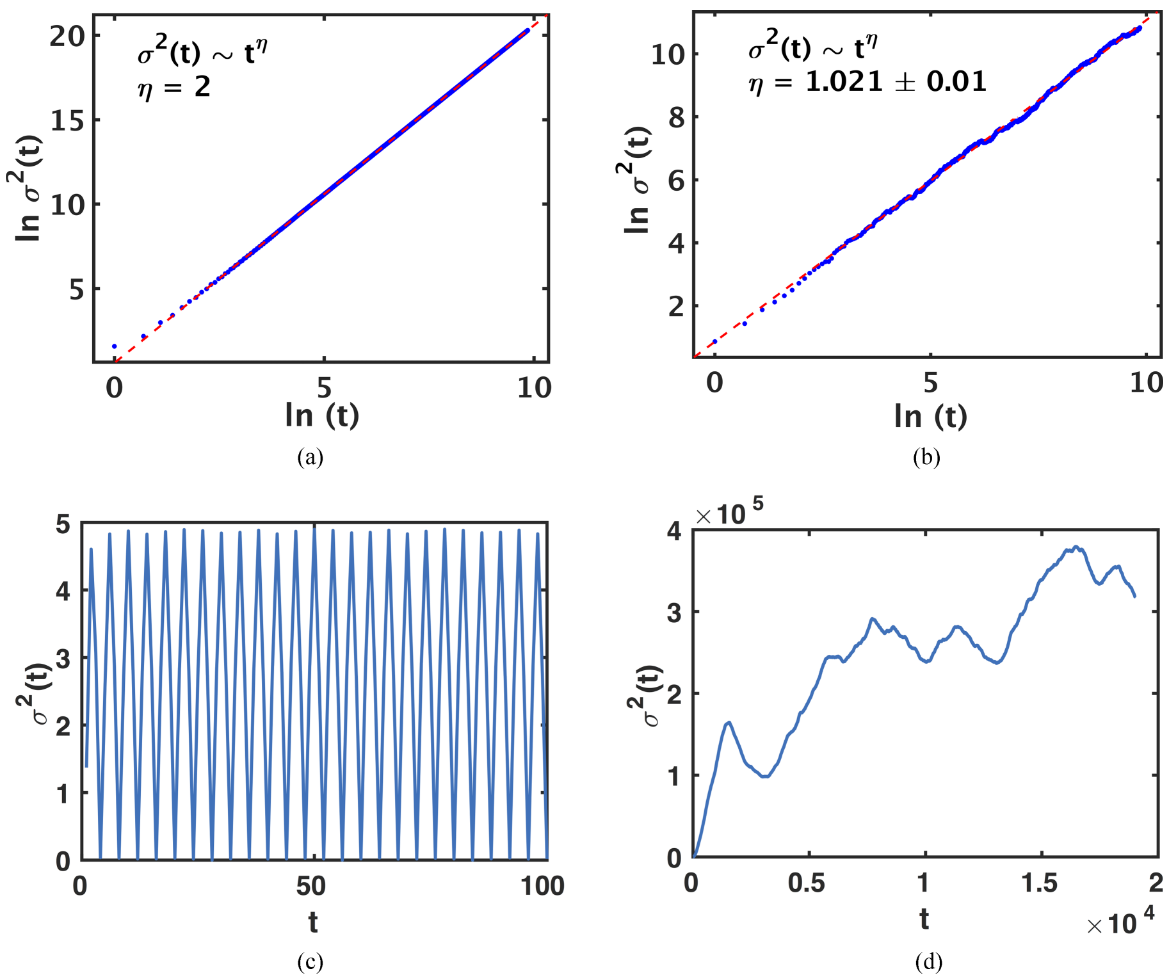

FIG. 4. The plots show the variance of the particle cloud evolving with time. (a) Superdiffusive behavior is observed at $(\alpha,\gamma) = (0.5,3.7)$. (b) A case of normal diffusion is seen at $(\alpha,\gamma) = (1.21,1.45)$. Trapping regimes show the plateauing of the variance—(c) with nonstationary states at $(\alpha,\gamma) = (0.33,1.17)$ and (d) stationary states at $(\alpha,\gamma) = (1.21,2.75)$. The stationary states are identified when $\eta < 0.92$ together with fluctuations in $\sigma^2(t)$ taking values below 1% during the last 2000 iterations.

discarded as transients. The trapping regions in the phase space wherein the stationary states appear in parts of the tubular regions. The trajectories therefore behave as if they get trapped in these attractors and their dispersion grows sublinearly with time. These states exist in the aerosol as well as bubble regimes.

To identify the normal diffusion regimes in a numerical computation, we choose a window where η values lie in the

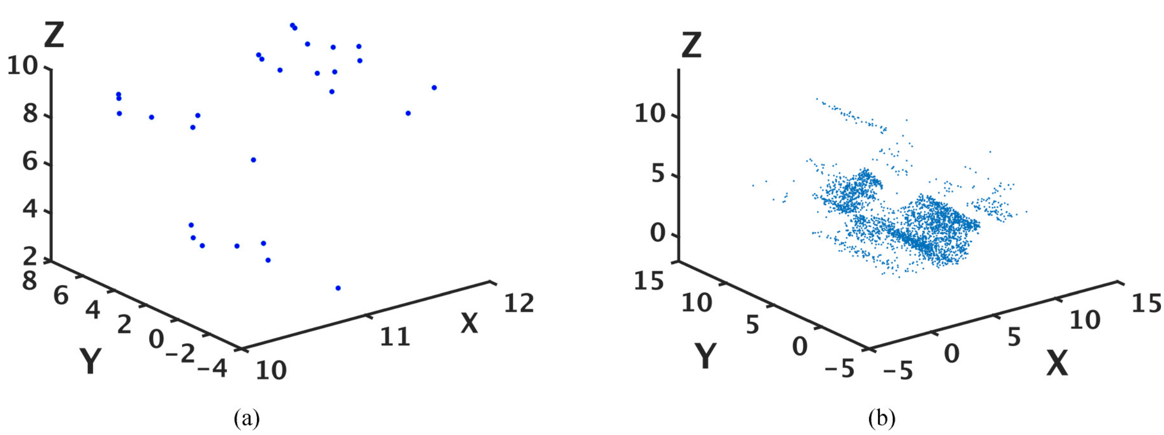

FIG. 5. The location of the attractor in the cover space for (a) nonstationary states at $(\alpha,\gamma) = (0.33,1.17)$ and (b) stationary states at $(\alpha,\gamma) = (1.21,2.75)$. The trajectories behave as though they are trapped in the neighborhood of these attractors and their dispersion grows sublinearly with time.

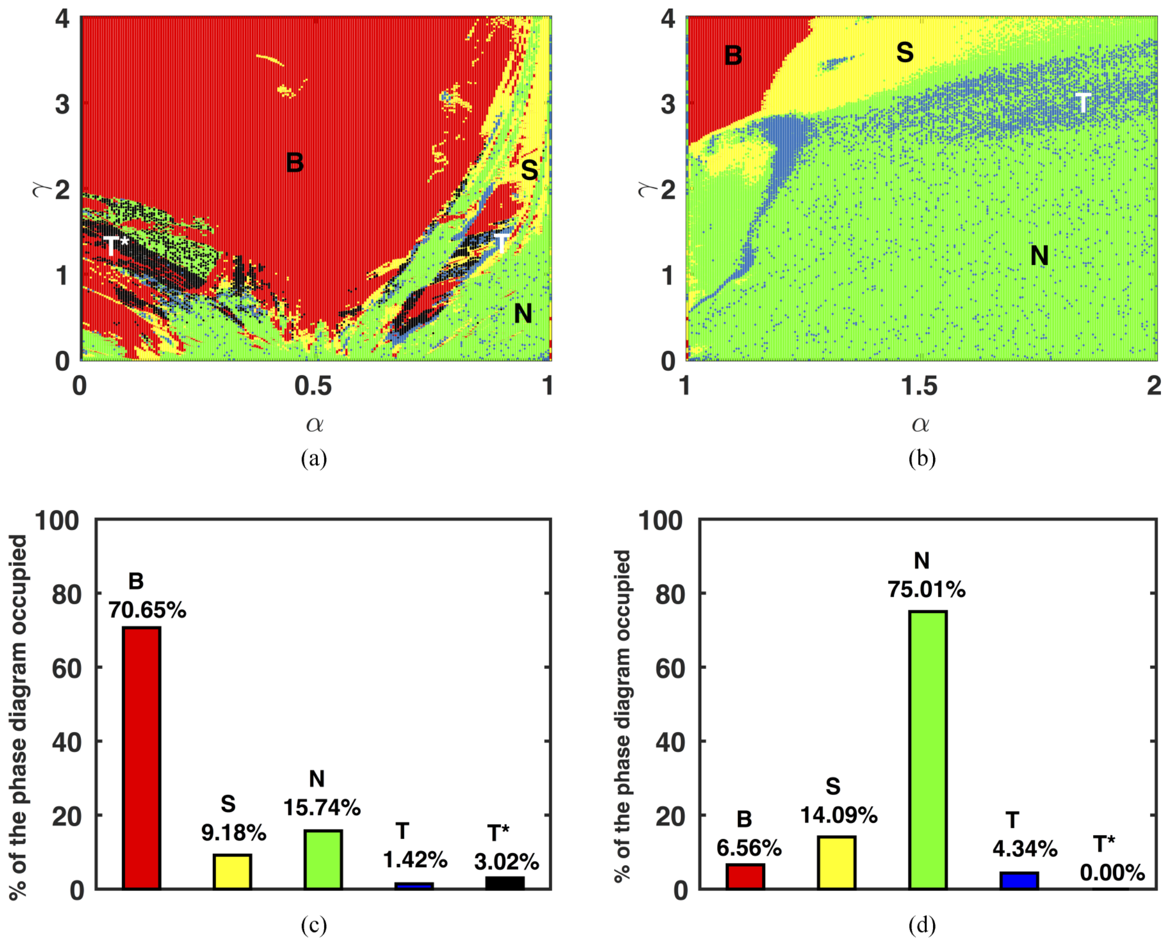

FIG. 6. The phase diagrams showing the four diffusion regions in the embedding map for the two-action case in the (α,γ) parameter space: the ballistic regime is marked by the color red with the label "B," the superdiffusive regime is marked in yellow with the label "S," normal diffusive regimes are marked in green with the label "N," subdiffusion with stationary states is marked in blue with the label "T," and subdiffusion with nonstationary states is shown by black with the label "T*." Panels (a) and (b) correspond to the aerosol regime and the bubble regime, respectively. The fraction of the phase space occupied by different diffusive regimes are indicated in (c) for the aerosol and (d) for the bubble regimes.

range $0.92 < \eta < 1.08$ to indicate normal diffusion in the system. Further, the superdiffusive and the ballistic regime are identified by the ranges $1.08 < \eta < 1.92$ and $1.92 < \eta < 2.12$, respectively. Ballistic diffusion (i.e., $\eta = 2$) has been seen in diverse contexts, such as the motion of atoms, molecules, and clusters on solid surfaces [43], and in random walk models with random velocities [44]. We now construct a phase diagram (Fig. 6) based on the values of the exponent of η using 10^4 iterations averaged over 200 trajectories. The diagram for the aerosol regime is shown in Fig. 6(a) and for that of the bubble regime in Fig. 6(b). The distribution of exponents is shown in Fig. 6(c) for the aerosol and in Fig. 6(d) for the bubble regime wherein two peaks are observed at about $\eta = 1$ and $\eta \approx 2$. The long tail in the window $1.05 < \eta < 1.98$ associated with larger peak at $\eta \approx 2$ has power-law scaling 1.429 ± 0.079 for the cumulative distribution as seen in Figs. 7(a) and 7(c). In the bubble regime, the long-tail associated with the larger peak at $\eta = 1$, in Figs. 7(b) and 7(d), plotted within $1.02 < \eta < 1.98$ has a power-law scaling with exponent 1.630 ± 0.055 for the reverse cumulative distribution.

We also show, for completeness, the corresponding phase diagram and fraction of the parameter space covered by different diffusive regimes for the one-action case in Fig. 8. Similar to the two-action case, the aerosol regime of the one-action case is dominated by the ballistic regime, which occupies about 67% of the available space, on the average. But, the subdiffusive regime stands at almost 15% of the whole, which is about three times that of the aerosol regime in the two-action case [Fig. 8(a)]. The corresponding fraction of stationary states is less than 10%, about one-third of that of the two-action case. The bubble regime of both the one- and the two-action cases have very similar phase diagrams [Figs. 8(b) and 6(b)]. There is a well-defined arch-like boundary between the superdiffusive and normal or subdiffusive regimes for higher values of (α,γ). The contribution of the subdiffusive regime is slightly above 10%.

The distributions of diffusion exponents for the one-action case in the aerosol regime and in the bubble regime are shown in Figs. 9(a) and 9(b). The long tails again show power-law scaling [see Figs. 9(c) and 9(d)]. The peaks here are smaller in size and demonstrate that the aerosol and the bubble regimes have a greater degree of heterogeneity. This is due to the fact that the one-action case of the ABC map has resonance sheets. These sheets get broken up in the embedded map version but

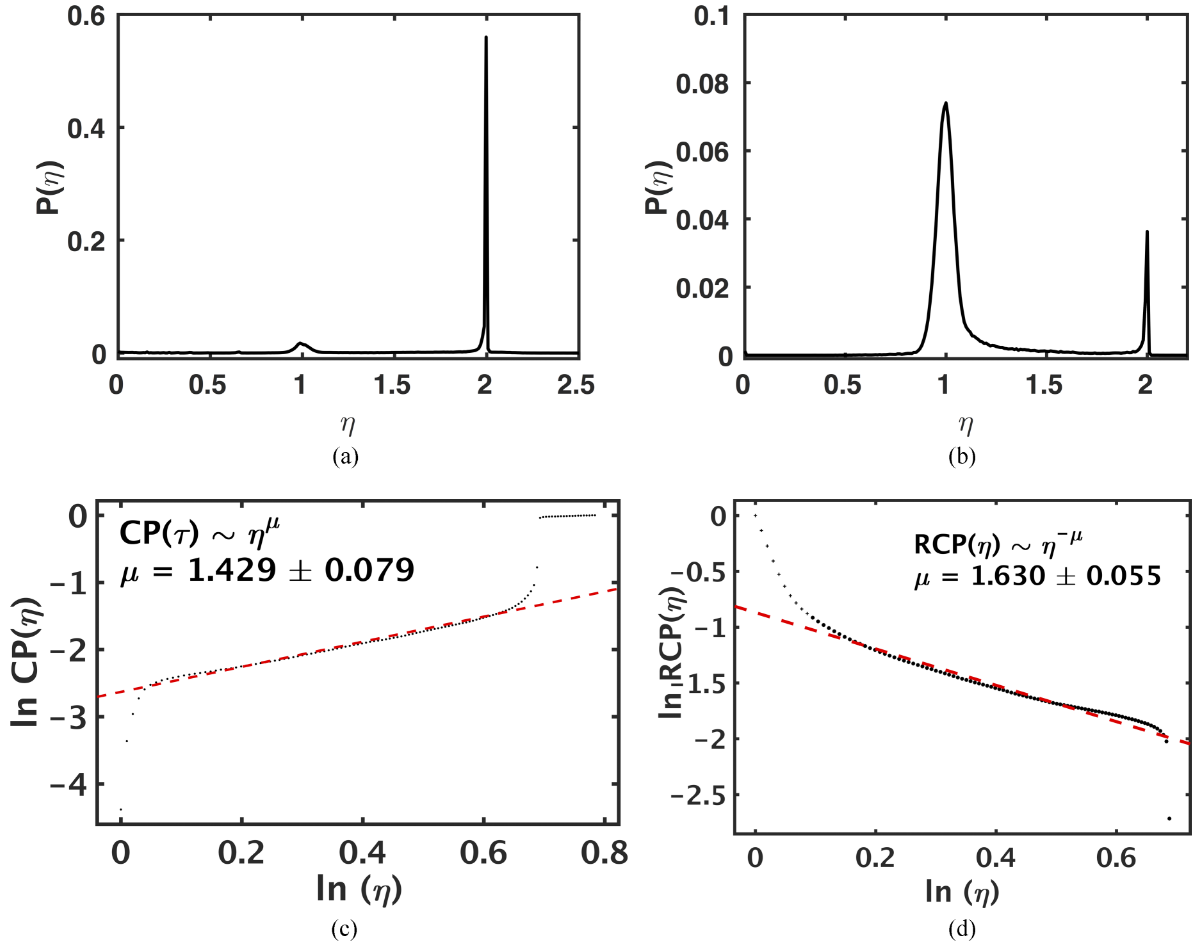

FIG. 7. The distribution of diffusion exponents for the two-action case in (a) the aerosol and (b) the bubble regimes. Power-law scaling is observed in the the long tail: (a) In the aerosol regime in the window $1.05 < \eta < 1.98$, associated with larger peak at $\eta \approx 2$, has power-law scaling 1.429 ± 0.079 for the cumulative distribution. (b) In the bubble regime, the long-tail associated with larger peak at $\eta = 1$, within $1.02 < \eta < 1.98$, has a power-law scaling with exponent 1.630 ± 0.055 for the reverse cumulative distribution.

influence the diffusion process of the trajectories in the cover space. In comparison, the two-action case where these sheets are absent shows global transport without constraints leading to a relatively less heterogeneous diffusion phase diagram.

Many of these behaviors are strongly influenced by the recurrence properties of the system. We now study the Poincaré recurrence times statistics to further characterize the transport behavior.

V. RECURRENCE TIME STATISTICS

The statistics of recurrence times in chaotic systems are of fundamental importance. These constitute the study of recurrences of a given dynamical system of the chaotic system in finite time. The recurrence time of a trajectory is defined as the time τ taken by the trajectory which starts from a small subset ξ of the phase-space Γ of the system to return to the same subset ξ, in the limit $\xi \to 0$ (see Fig. 10). The recurrence time corresponding to the ith recurrence is denoted by τ_i. The distribution of recurrence times $\tau_1, \tau_2, \ldots, \tau_n$ for a trajectory may thus be obtained in the long time limit. The average recurrence time of the subset ξ is calculated by averaging over the recurrence times of the trajectories starting in the subset, and the average recurrence time of the entire phase-space Γ can be obtained by averaging over the recurrence times of all such subsets in the phase space (see Refs. [45,46] for more rigorous definitions).

Mean recurrence times in low-dimensional Hamiltonian systems have been studied extensively. The phase space of area-preserving systems commonly exhibits mixed phase space; i.e., regular structures and chaotic regions may co-exist. The interfaces of these chaotic regions and regular orbits are complex causing the trajectories to spend longer times in these neighborhoods. A major consequence of this "stickiness" is the existence of power laws in the Poincaré recurrence times, indicating algebraic decay for long times rather than the exponential decay expected for normal transport. The quantity of interest here is the cumulative probability distribution $P_{\rm cum}(\tau)$ defined by

$$P_{\rm cum}(\tau) = \sum_{\tau'=\tau}^{\infty} P(\tau'). \tag{8}$$

Straight lines in the log-log plot of this distribution indicate power-law decays of the form $P_{\rm cum}(\tau) \sim \tau^{-\beta}$, where β is the decay exponent.

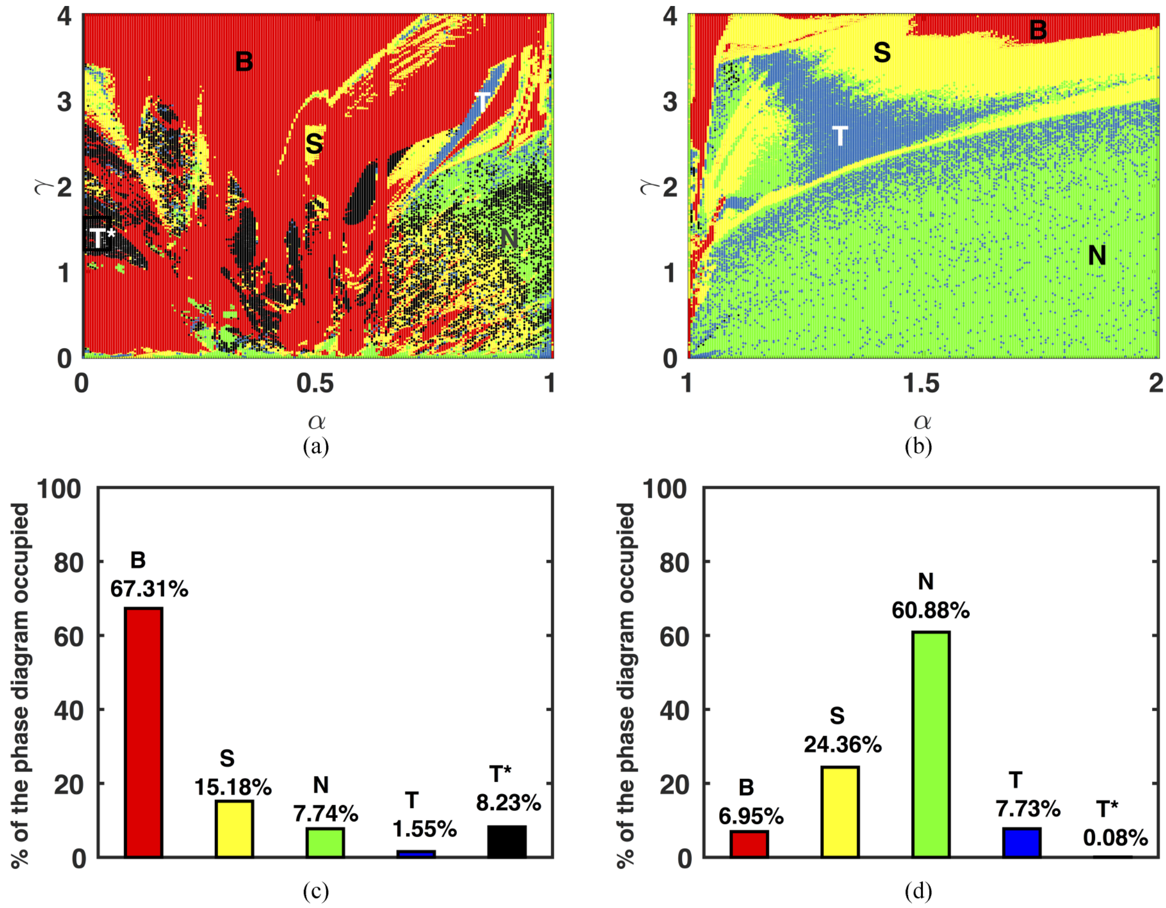

FIG. 8. The phase diagrams showing the four diffusion regions in the embedding map for the one-action case in the (α,γ) parameter space: the ballistic regime is marked by the color red with the label "B," the superdiffusive regime is marked in yellow with the label "S," the normal diffusive regimes are marked in green with the label "N," subdiffusion with stationary states is marked by the color blue with the label "T," and subdiffusion with nonstationary states is shown in black with the label "T*." Panel (a) shows the aerosol regime, and panel (b) shows the bubble regime. The fraction of the phase space occupied by different diffusive regimes are indicated in (c) for the aerosol and (d) for the bubble regimes.

We apply recurrence time statistics to the embedding of the ABC map. The computations for recurrence times have been performed for 3D recurrences in the X-Y-Z configuration space. The phase space is divided into a grid comprising of $50 \times 50 \times 50$ cells, each of size $0.02 \times 0.02 \times 0.02$ units. We compute the recurrences after 10^7 iterations with 1000 iterates discarded as transients. All the values of (X,Y,Z) were normalized by 2π in the interval [0,1]. The mean recurrence time for each cell c is given by

$$\langle\tau\rangle_c = \frac{1}{N(r)}\sum_{i=1}^{N(r)}\tau_i. \tag{9}$$

Here, $N(r)$ indicates the total number of recurrences in a given cell. The resulting cumulative probability distributions of recurrence times are shown in Fig. 11.

These distributions depend upon the nature of the dynamics at the given set of parameter (α,γ). The trajectories in both the aerosol and bubble regimes may breach the invariant regions or get pushed away from them. The complete breach of the invariant surfaces, in the embedded system, leads to global transport with chaotic or hyperchaotic dynamics. For our study here, we choose a set of four pairs of parameters (α,γ); two for both the two- and the one-action cases. Figures 11(a) and 11(b) show the decay for the two-action case at $(\alpha,\gamma) = (1.6,3.7)$ (hyperchaotic) and (0.9,1.0) (chaotic) at parameter values $(A,B,C) = (2,1.5,0.08)$.

We will continue the discussion with special attention to the example drawn from the hyperchaotic regime of the two-action case. The trajectories visit the neighborhood of the invariant tubes of the two-action base map and experiences stickiness (see Fig. 12). The darker regions on the $Y = 0.5$ plane indicate that trajectories tend to spend longer times in the area surrounding the invariant surfaces corresponding to the base ABC map. Notice that in Fig. 12, largely unpenetrated elliptic regions are seen that envelop the tubular regions of the base ABC map indicated by periodic orbits on the slice (in color "red").

It has been observed that algebraic decays of recurrence times are seen in area-preserving systems due to the occurrence of partial barriers [47,48] in the form of Cantori, which form hierarchical structures around the principal regular island. Unlike this situation, the mechanism that contributes to algebraic decays in the recurrence times in the embedded map system here does not appear to be the existence of a hierarchy in the phase space. This observation is similar to that reported

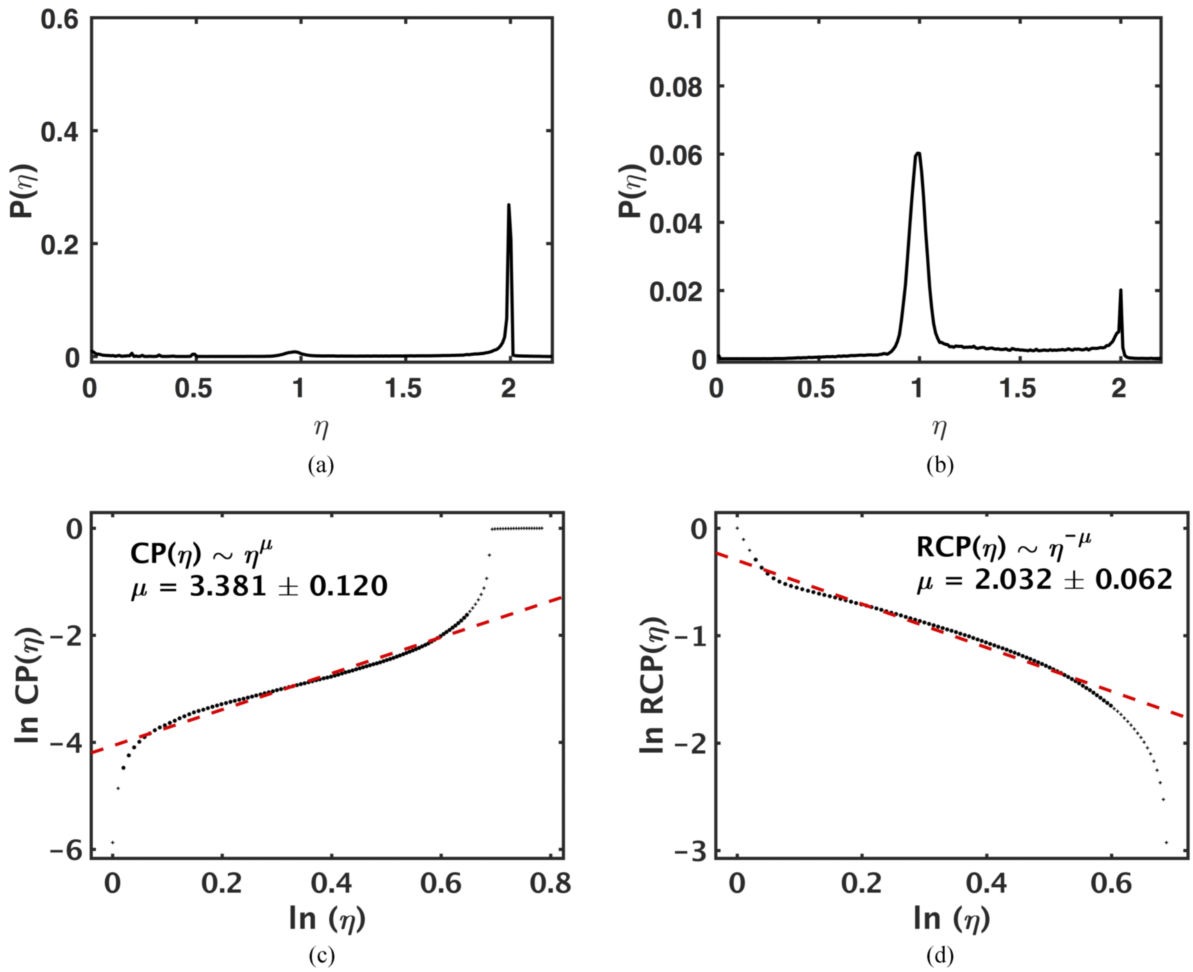

FIG. 9. The distribution of diffusion exponents for the one-action case in (a) the aerosol and (b) the bubble regimes. Power-law scaling is observed in the long tail in diffusion exponent distribution. (a) In the aerosol regime in the window $1.01 < \eta < 1.92$, associated with larger peak at $\eta \approx 2$, has power-law scaling 3.381 ± 0.120 for the cumulative distribution. (b) In the bubble regime, the long-tail associated with larger peak at $\eta = 1$, within $1.02 < \eta < 1.82$, has a power-law scaling with exponent 2.032 ± 0.062 for the reverse cumulative distribution.

recently [49], where it has been demonstrated that in the case of a 4D symplectic map, the trapping does not take place due to hierarchy of satellite islands in phase space but occurs at the surface of regular regions and also outside of the Arnold web.

Another important aspect of the decay curve to be noted is that the distributions display plateaus in Fig. 11. Similar distributions with plateaus were seen in a 3D volume preserving extended standard map [50]. The plateaus indicate that the trajectories are evolving for longer times, as no recurrences occur within the number of iterations computed. The long recurrences observed here are due to the surviving trapping effects of the invariant tubes of the base two-action map. Similar trapping effects are observed in Ref. [50], wherein a non-Hamiltonian volume-preserving map has been studied.

We also note that the one-action case also shows similar decay of recurrence times embedded with plateaus in Figs. 11(c) and 11(d) for $(\alpha,\gamma) = (1.85,3.2)$ and $(0.85,2.0)$, respectively. However, the transport in the one-action case is more complicated than the two-action case, owing to the existence of invariant sheets. The probability distribution of recurrence times shows heavy tails, but the location of the sticky regions is not as clear as in the two-action case. It is highly likely that the invariant surfaces act as partial barriers and influence the transport process. Therefore, the mechanisms

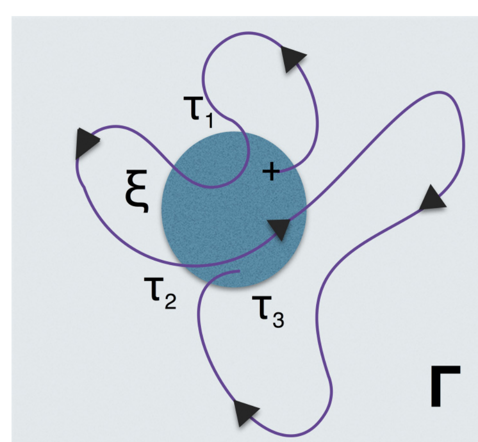

FIG. 10. The schematic illustration of the recurrence phenomena in an invariant set Γ. A trajectory starting in a small subset ξ is revisiting the subset in finite time. The diagram shows only the first three recurrences corresponding to recurrence times τ_1, τ_2, and τ_3.

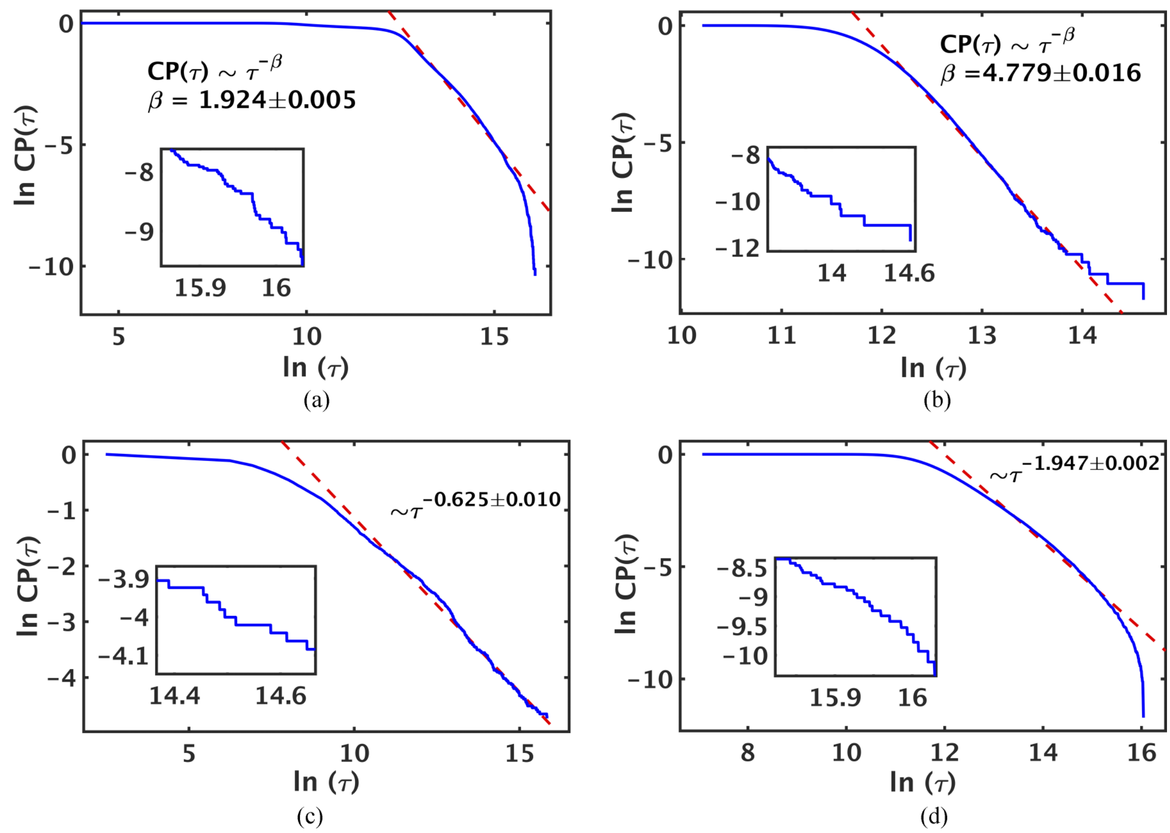

FIG. 11. Recurrence time distributions in (a) the hyperchaotic regime $(\alpha,\gamma) = (1.6,3.7)$ for the two-action case (b) the chaotic regime $(\alpha,\gamma) = (0.9,1)$ for the two-action case, (c) the hyperchaotic regime $(\alpha,\gamma) = (1.85,3.2)$ for the one-action case, and (d) the chaotic regime $(\alpha,\gamma) = (0.85,2.0)$ for the one-action case. The plateaus indicate very long recurrences due to the trapping of particles in the tubular regions.

suggested in Ref. [49] appear to be at work in the embedded map too. However, a detailed study is required to establish the exact mechanism of the trapping behavior conclusively.

VI. CONNECTION BETWEEN THE DYNAMICAL BEHAVIORS AND TRANSPORT PROPERTIES

The discussion so far indicates an intimate connection between the dynamical behavior and the statistical properties of the system. In this section, we outline the important inferences.

As stated earlier, the phase diagram for the dynamical regimes of the embedded ABC map, a paradigm for the dynamics of inertial particles in 3D fluid flows, contains three distinct dynamical regimes, viz., periodic orbits, chaotic structures, and hyperchaotic behavior. The dynamics also differentiates between the aerosol and bubble regime. Figure 13 shows the phase diagram for the two-action case that was reported in our earlier work [28] (see Fig. 2 for the phase diagram for the one-action case).

In Sec. IV, we constructed the phase diagrams in α-γ parameter space that encapsulate the diffusive behaviors in the system. Once again, distinctly different behaviors, viz., subdiffusive, normal, i.e., of the Brownian type, and superdiffusive, including ballistic behavior, were observed for the aerosol and the bubble regimes in both the cases.

We first discuss the two-action case. In the diffusion phase diagram, the aerosol regime is clearly dominated by ballistic

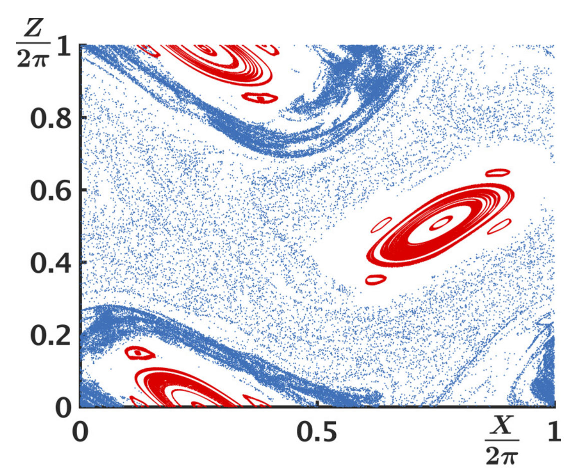

FIG. 12. This figure demonstrates the stickiness of the trajectories around the tubes in the embedded two-action case in the hyperchaotic regime at $(\alpha,\gamma) = (1.6,3.7)$. The plot shows the X-Z space at the $Y = 0.5$ plane. The darker regions correspond to the neighborhoods of the invariant tubes of the base ABC map. Trajectories wander inside the tubes briefly, resulting in plateaus in the corresponding recurrence time distribution. Regular structures and islands in red indicate the elliptical invariant regions in the base ABC map (two-action) [see Fig. 1(d)].

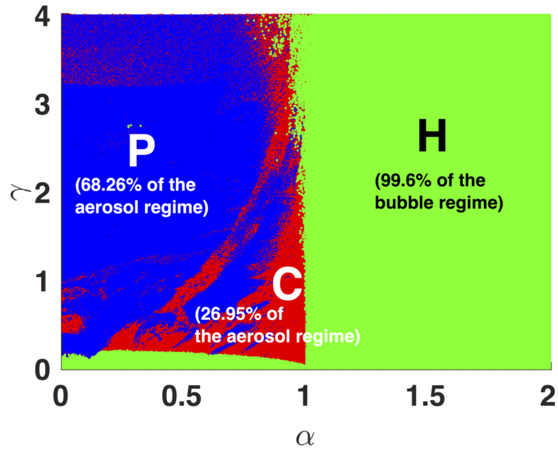

FIG. 13. The phase diagram of the embedded two-action ABC map for parameter values $(A,B,C) = (2.0,1.3,0.16)$ [periodic orbits, blue (P); chaotic behavior, red (C); hyperchaotic regions, green (H)]. The α-γ space is covered by a 400×800 mesh, each of size 0.005×0.005. A total of 25 000 iterates have been calculated in each case. The phase diagram has been plotted for 25 000 iterates discarding first 5000 iterates as transients.

transport covering over 70% of the parameter space. The dynamical behavior in this regime shows largely periodic nature. In addition, the chaotic structures and hyperchaotic behavior here are correlated with normal diffusion and superdiffusion. The superdiffusive regime overall occupies about 9% of the phase diagram, whereas 16% of the diagram shows normal diffusive behavior. The region with the greater degree of heterogeneity in the neighborhood of $\alpha > 0.7$ corresponds mostly to the chaotic structures and regions where both chaotic and periodic behavior coexist in the phase space. Small traces of subdiffusive transport also exist in the aerosol regime, which mostly correspond to the region with periodic dynamics. The subdiffusive region is approximately the region that contains nonstationary states. We note that, in the one-action case, however, the subdiffusive regimes occupy a larger area, comprising about 10% of the phase diagram.

On the other hand, normal diffusion is prominent in the bubble regime occupying about 75% of the space. This regime is almost completely hyperchaotic. Superdiffusive transport is limited to higher values of dissipation in a region with a diffuse boundary, and an additional narrow channel nearly spanning the full range of α. The ballistic regime is much smaller than that seen in the aerosol case and covers about 7%. The superdiffusive regions occupies about 14% of the space. The fraction of subdiffusive regimes remain at about 8% but the contribution of stationary states rises to almost 99% of the subdiffusive regions. Stationary states are those for which the variance remains below 1%. Therefore, the subdiffusive behavior emerging here is that trapped states are mostly nonstationary in the aerosol regime, whereas the stationary states prevail over nonstationary states in the bubble regime. This may lead to regions of preferential concentration, as seen in the case of studies in the 2D case [19,41], which showed that bubbles may get pushed toward the islands forming regions of preferential concentration. Trapping states in the aerosol regime has also been noted in other works [42].

Our analysis for Poincaré recurrence times in Sec. V showed that chaotic and hyperchaotic regimes contain trajectories that display sticky behavior in the phase space. The corresponding recurrence times statistics show power-law tails in addition to the expected exponential decays as seen in the previous section. Such power-law trapping has significant consequences for chaotic transport in a variety of systems. Examples of these include the three-body problem [51], in dynamics due to the Caldera potential in organic chemical reactions [52], driven coupled Morse oscillators [53], etc. We now study the energetic properties of inertial particles in the embedded ABC map.

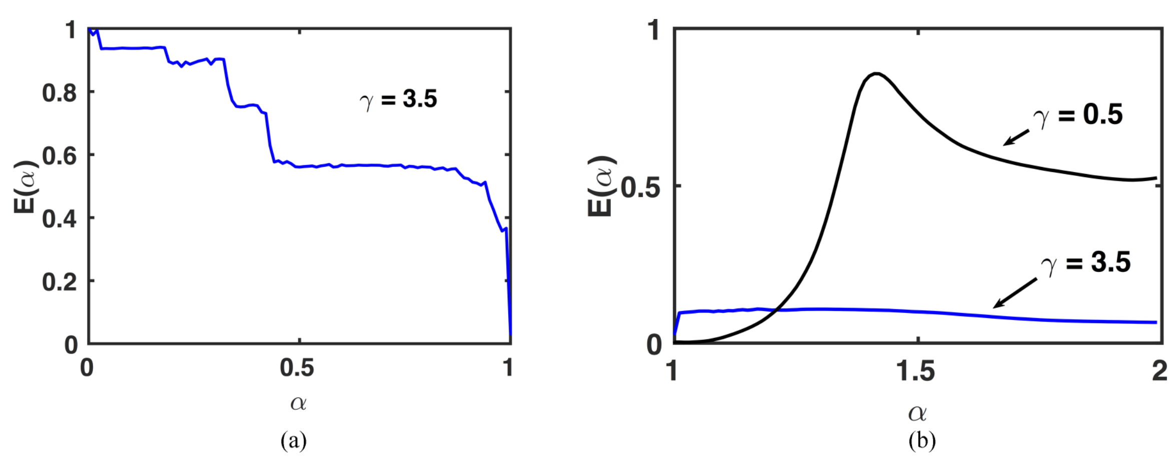

FIG. 14. (a) Self-similar staircase in the variation of $\langle E(\alpha)\rangle$ for the aerosol regime in the two-action case at $\gamma = 3.5$. These jumps in $\langle E(\alpha)\rangle$ indicate that the particles move on trajectories confined inside different tubes with increasing α. (b) The corresponding bubble regime shows entirely different behavior. For $\gamma = 3.5$, the energies are small due to the fact that the trajectories get concentrated around the invariant tubes, whereas for $\gamma = 0.5$, the trajectories transport over the entire phase space. The one-action case shows similar behavior. The energy values have been computed for 10 000 iterations and averaged over 200 particles.

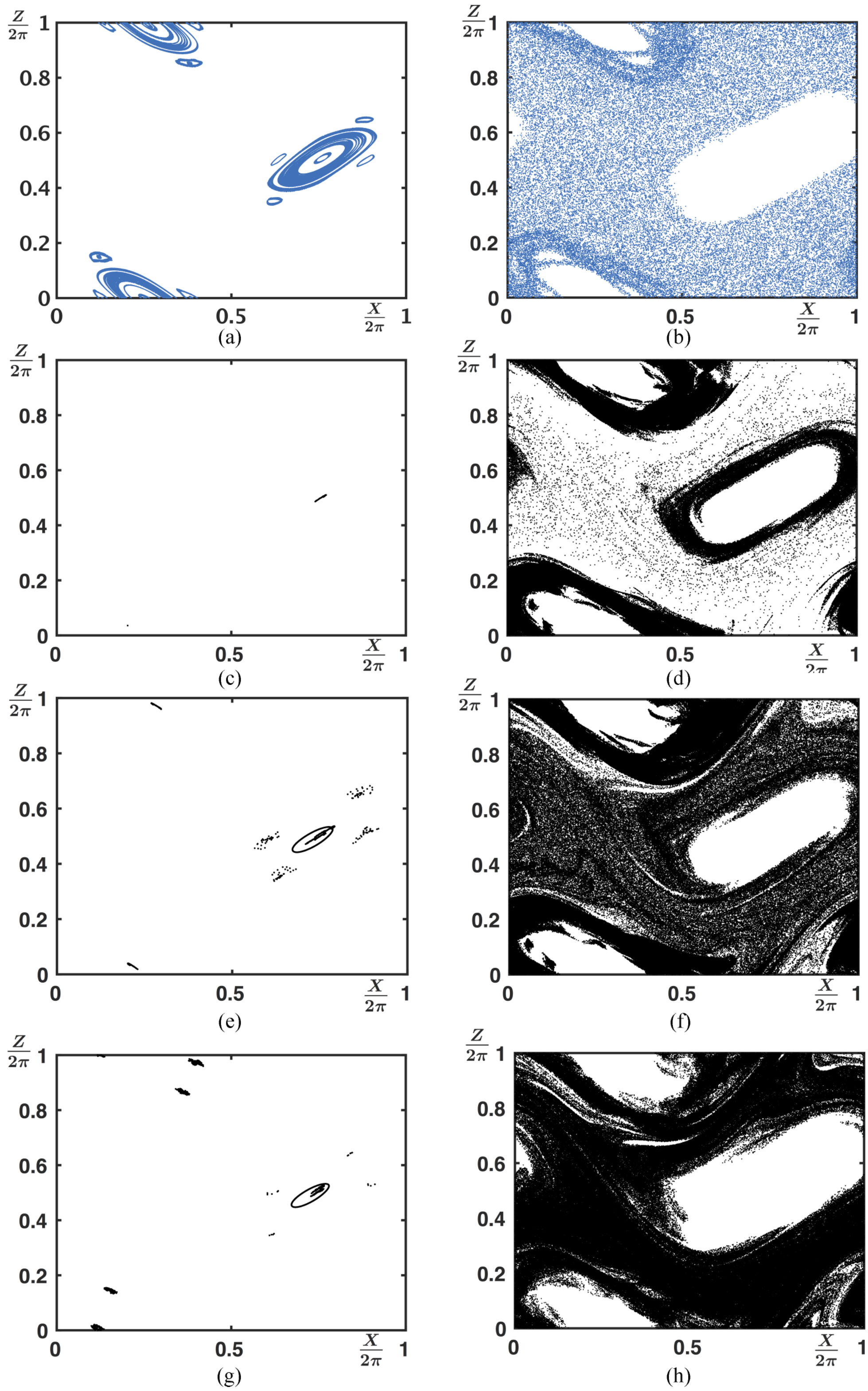

FIG. 15. All the plots show the $Y = 0.5$ plane. The left panel: (a) regular regions in the ABC map; (c), (e), and (g) show the phase space of the embedded ABC map in the aerosol regime for $\alpha = \{0.25, 0.60, 0.75\}$, respectively, at $\gamma = 3.5$. The trajectories go inside the regular regions. The right panel: (b) chaotic regime in the ABC map; (d), (f), and (h) show the phase space of the embedded ABC map in the bubble regime for $\alpha = \{1.25, 1.50, 1.80\}$, respectively at $\gamma = 3.5$. The trajectories are expelled out of the regular regions.

VII. ENERGY STUDIES

We now move to study the energy associated with the passive scalars in the embedded map dynamics. We examine a specific contribution to the kinetic energy here, viz. we study the quadratic contribution to the average kinetic energy of the system, at given value of the dissipation parameter γ, due to the relative velocity of the particles. This may be defined as

$$E(\alpha) = \left\langle \tfrac{1}{2}\delta^2(\alpha) \right\rangle. \tag{10}$$

Here δ indicates the relative velocity of the passive particles immersed in the fluid flow, as in Eq. (4), we have defined δ to be the detachment from the fluid velocity. The angular brackets $\langle \ldots \rangle$ indicate the ensemble average. We examine both the aerosol regime ($\alpha < 1$) as well as the bubble regime ($\gamma > 1$). The most interesting behavior of the energy values with respect to α in both the regimes for the two-action case is shown in Fig. 14. In Fig. 14(a), at $\gamma = 3.5$, several plateaus are visible that in fact have self-similar nature on small scales reminiscent of a devil's staircase. From the configurational space dynamics of the particles, we know that at higher dissipation values, particles in the aerosol regimes are trapped inside the tubular regions of the base ABC map. The plots on the top of Figs. 15(a) and 15(b) show regular and chaotic regions, respectively, on the $Y = 0.5$ plane for the base ABC map. With α increasing from values toward 1, the particle trajectories get confined inside successive nested surfaces inside the tubular regions (see Figs. 15(c), 15(e) and 15(g) for $\alpha = \{0.25, 0.60, 0.75\}$, respectively) until $\alpha = 1$. These successive "jumps" are reflected in the staircase structures of the curve in Fig. 14(a). The bubble regimes (Figs. 15(d), 15(f) and 15(h) for $\alpha = \{1.25, 1.50, 1.80\}$, respectively) show that the trajectories always lie outside the regular regions. No curves of the staircase type are observed in the bubble regime.

On the other hand, the bubble regimes behave in a completely different manner. For larger values of dissipation, see Fig. 14(b), the energies remain small and largely constant. The trajectories corresponding to these energies are concentrated outside the invariant tubes and therefore their energies are largely constant and small. However, for smaller values of dissipation, such as $\gamma = 0.5$ in Fig. 14(b), trajectories are initially outside the invariant tubes but access the regions of the phase space inside the tubes once the dissipation rises. The energy rises and reaches an almost constant level once the penetration is complete, leading to global transport of the trajectories. The fundamental difference to be noted is that the trajectories in the bubble regime, for higher dissipation, always remain outside the tubular regions and do not appear to leave this vicinity but, for smaller dissipation, the trajectories evolve throughout the phase space outside the tubular regions only at small α. With increase in α, they start to penetrate the tubes until global transport is complete.

The one-action case shows largely similar behavior in both, aerosol and bubble regimes. In the aerosol regime, however, the behavior in not as conspicuous as the phase space of the base map has layers of resonance sheets in addition to tubes. The phase space is divided by these sheets and at higher values of dissipation, the trajectories may either stay close to them or end up inside the tubular regions. Therefore, the staircase structure of the energy curve is destroyed by the trajectories outside the invariant tubes.

VIII. CONCLUSIONS

In this work, we have described the transport, diffusion, and energetic properties of passive scalars in a volume-preserving ABC map under the embedded map model. The model encapsulates the dynamics of impurities in a 3D chaotic fluid wherein the density of impurities differ from that of the fluid parcels. Consequently, the trajectories of impurity particles separate from those of the fluid resulting in highly complex dynamics. The complexity primarily arises due to the mixed nature of the phase space of the ABC map, which contains invariant surfaces as well as chaotic trajectories in the bulk of the phase space. The embedded dynamics also depends on the parameters (α, γ), which correspond to the mass ratio and the dissipation in the system, with the mass ratio α distinguishing between the aerosol ($\alpha < 1$) and bubble ($\alpha > 1$) regimes, which display qualitatively different dynamical behavior.

We have considered the two-action and the one-action versions of the base ABC map. The focus has been on the former, wherein a higher efficiency of mixing is expected due to the absence of invariant barriers. The phase spaces in both aerosol and bubble regimes show rich and complex dynamics with three types of dynamical behaviors—chaotic structures, regular orbits, and hyperchaotic regions. We have observed that the bubble regimes in the one-action and two-action cases display bipartite attractors with interesting return times statistics. The tendency of the sticking of chaotic trajectories to some phase-space regions for long times as indicated by power-law decays in the recurrence times statistics and has been earlier seen in the case of low-dimensional Hamiltonian systems, is found to be present in our system as well. However, unlike the 2D cases, such partial barriers to transport in our system do not appear to originate from hierarchical structures in the phase space. Instead, in the hyperchaotic regime, for $\gamma > 2$, such sticky regions exist around the invariant surfaces for the two-action case. An analogous case has been seen in a 4D symplectic map [49] where the power law trapping of the trajectories is not due to a hierarchy in phase space, but occurs at the surface of the regular region and outside of the Arnold web. Moreover, we observe plateaus in the recurrence time distributions indicating longer recurrence times inside the trapping regions. Such plateaus have been reported earlier in the volume preserving extended standard map [50].

The system also exhibits the entire range of diffusive properties including normal diffusion, subdiffusion and superdiffusion. The aerosol regime is mostly dominated by the ballistic type of superdiffusion while in the bubble regime, the largest fraction of the available parameter space is occupied by normal diffusion. The distribution of diffusion exponents in the two-action case shows power-law scaling over a certain range in both the aerosol and the bubble regimes. We also observe a clear boundary between the normal and superdiffusive regions in the bubble regime. The degree of heterogeneity in the phase diagram of the one-action case is greater than that of the two-action case. This is expected due to the fact that more invariant surfaces get destroyed in the one-action case.

Our energy studies show that the energy associated with the passive scalars in the embedded map dynamics also shows structure, the specific quantity under study being $E(\alpha)$, the quadratic contribution to the kinetic energy due to the separation between the impurity and the fluid velocities. In the two-action case, the variation of $E(\alpha)$ in the aerosol regime shows the existence of plateaus which resemble the devil's staircase. The trajectories here, are localized in invariant tubular regions, and move through the energy surfaces inside the tube with increase in α. This behavior results in the staircase type of behavior in the energy curve. On the other hand, trajectories in the bubble regime either breach the invariant surfaces (for small values of γ) or are completely expelled out of them (for higher values of γ) leading to the absence of any plateaus in the energy curve. Finally, we note, as expected, the existence of invariant sheets alters the behavior in the one-action case where a clear picture of diffusion and transport dynamics as well as energies does not emerge unlike the two-action case.

It is to be clarified that the bailout embedding of particles ignores the memory effects (as modeled by the Basset history force term) seen in the dynamics of inertial particles. It has recently been shown that these effects have important influences on the chaotic advection of bubbles as well as aerosols in the 2D von Kármán flow [54–56] leading to phenomena like changing the nature and number of attractors, the fractalization of basin boundaries, and weakening of the diffusive effects. It would, therefore, be interesting to see the ramifications of the history term for inertial particle advection in 3D flows as well.

We now discuss the implications of our study. The transport and diffusive properties of impurities in a three-dimensional volume preserving map have been explored in detail, using the embedded map paradigm. Such 3D volume preserving maps are representations of time-periodic flows in three dimensions. Early studies [15,16] of bailout embeddings of the ABC map investigate the neutrally buoyant ($\alpha = 1$) case and also study the effects of noise. We hope to study these effects of noise for our $\alpha \neq 1$ case elsewhere.

The specific map used here, is a map representation of the ABC flow, which models cosmic magnetic fields [57–59]. The ABC map serves as as a paradigm for studying the spatial diffusion of the magnetic field lines in astrophysical plasmas. The conventional approach to describe the transport of particles in plasmas involves the classical theory of random walks. We, however, have seen that anomalous diffusion is not only present in the our model, but is predominant in a certain region of the parameter space. Similar results have been obtained in recent work [60]. Also, the recurrences of states are non trivial and may have definite consequences for the evolution of magnetic fields in plasma. We have also distinguished between the two- and one-action cases, which have been not explored yet in the context of kinematic dynamo model. Therefore, we hope that the insights gained here would be useful in this, and other application contexts.

APPENDIX: THE MAXEY-RILEY EQUATIONS AND THE BAILOUT EMBEDDING MAP

The transport of passive point particle tracers in fluids is usually studied using the Lagrangian description, wherein the particle advection problem is expressed as a finite-dimensional dynamical system. If the density of the particle tracers is different from that of the fluid, the problem needs to be tackled using the Maxey-Riley framework [29], which involves a series of simplifying assumptions [35]. These equations are

$$\begin{aligned}\rho_p \frac{d\mathbf{v}}{dt} &= \rho_f \frac{d\mathbf{u}}{dt} + (\rho_p - \rho_f)g - \frac{9\nu\rho_f}{2a^2}\left(\mathbf{v} - \mathbf{u} - \frac{a^2}{6}\nabla^2\mathbf{u}\right)\\ &\quad - \frac{\rho_f}{2}\left(\frac{d\mathbf{v}}{dt} - \frac{D}{Dt}\left[\mathbf{u} + \frac{a^2}{10}\nabla^2\mathbf{u}\right]\right)\\ &\quad - \frac{9\rho_f}{2a}\sqrt{\frac{\nu}{\pi}}\int_0^t \frac{1}{\sqrt{(t-\xi)}}\frac{d}{d\xi}\left(\mathbf{v} - \mathbf{u} - \frac{a^2}{6}\nabla^2\mathbf{u}\right)d\xi.\end{aligned} \tag{A1}$$

Here $\mathbf{v}$ represents the particle velocity, $\mathbf{u}$ the fluid velocity, ρ_p the density of the particle, ρ_f the density of the fluid, and ν, a, and $\mathbf{g}$ represent the kinematic viscosity of the fluid, the radius of the particle and the acceleration due to gravity, respectively. The first term on the right of Eq. (A1) represents the force exerted by the undisturbed flow on the particle, the second term represents the buoyancy, the third term represents the Stokes drag, the fourth term represents the added mass, and the last term is the Basset-Boussinesq history force term. The two derivatives involved in the equation, $\frac{D\mathbf{u}}{dt}$ and $\frac{d\mathbf{u}}{dt}$, are defined as follows:

$$\frac{D\mathbf{u}}{Dt} = \frac{\partial \mathbf{u}}{\partial t} + (\mathbf{u}\nabla)\mathbf{u}, \tag{A2}$$

$$\frac{d\mathbf{u}}{dt} = \frac{\partial \mathbf{u}}{\partial t} + (\mathbf{v}\nabla)\mathbf{u}. \tag{A3}$$

The derivatives $\frac{D\mathbf{u}}{dt}$ and $\frac{d\mathbf{u}}{dt}$ are taken along the path of the fluid element and the trajectory of the particle, respectively.

In this framework, we arrive at the following simplified equation of motion for the motion of a spherical particle immersed in the fluid [27], under the low Reynolds number approximation, with negligible buoyancy effects, and retaining only the Bernoulli, Stokes drag, and Taylor added terms:

$$\frac{d\mathbf{v}}{dt} - \alpha\frac{d\mathbf{u}}{dt} = -\frac{2}{3}\left(\frac{9\alpha}{2a^2\mathrm{Re}}\right)(\mathbf{v} - \mathbf{u}). \tag{A4}$$

Here, the parameter α is the mass density ratio, $\alpha = \frac{\rho_f}{\rho_f + 2\rho_p}$, corresponding to the aerosol case ($\alpha < 1$), the bubble case ($\alpha > 1$), and the neutrally buoyant cases ($\alpha = 1$). Defining the particle Stoke's number $\mathrm{St} = \frac{2}{9}a^2\mathrm{Re}$ and defining the dissipation parameter to be $\gamma = \frac{2\alpha}{3\mathrm{St}}$, the equation takes the form

$$\frac{d\mathbf{v}}{dt} - \alpha\frac{d\mathbf{u}}{dt} = -\gamma(\mathbf{v} - \mathbf{u}). \tag{A5}$$

A map version of this bailout embedding is given by Eq. (2) in Sec. II.

[1] W. H. Snyder, Annu. Rev. Fluid Mech. **17**, 239 (1985).
[2] M. A. Fogleman, M. J. Fawcett, and T. H. Solomon, Phys. Rev. E **63**, 020101 (2001).
[3] W. L. Vargas, L. E. Palacio, and D. M. Dominguez, Phys. Rev. E **67**, 026314 (2003).
[4] E. A. Ryzhov and K. V. Koshel', Izv. Atmos. Ocean. Phys. **46**, 184 (2010).
[5] E. A. Ryzhov, K. V. Koshel, and X. J. Carton, Eur. J. Mech. B-Fluid **34**, 121 (2012).
[6] R. E. Newell, V. Thouret, J. Y. N. Cho, P. Stoller, A. Marenco, and H. G. Smit, Nature **398**, 316 (1999).
[7] P. Haynes, *Transport, Stirring, and Mixing in the Atmosphere* (Springer, Boston, MA, 1999), pp. 229–272.
[8] J. Laskar, Icarus **196**, 1 (2008).
[9] R. B. Bird, W. E. Stewart, and E. N. Lightfoot, *Transport Phenomena, Revised 2nd Edition* (Wiley, New York, 2006).
[10] C. A. Shook and M. C. Roco, *Slurry Flow: Principles and Practice* (Elsevier, New York, 2015).
[11] J. M. Ottino, *The Kinematics of Mixing: Stretching, Chaos, and Transport*, Cambridge Texts in Applied Mathematics (Cambridge University Press, Cambridge, 1989).
[12] R. T. Pierrehumbert, Phys. Fluids A **3**, 1250 (1991).
[13] H. Aref, Phys. Fluids **14**, 1315 (2002).
[14] J. H. E. Cartwright, M. O. Magnasco, and O. Piro, Phys. Rev. E **65**, 045203(R) (2002).
[15] J. H. E. Cartwright, M. O. Magnasco, O. Piro, and I. Tuval, Phys. Rev. Lett. **89**, 264501 (2002).
[16] I. Tuval, Ph.D. thesis, Universitat de les Illes Balears, 2005.
[17] R. Sturman, J. M. Ottino, and S. Wiggins, *The Mathematical Foundations of Mixing* (Cambridge University Press, Cambridge, 2006).
[18] N. N. Thyagu and N. Gupte, Phys. Rev. E **76**, 046218 (2007).
[19] N. Nirmal Thyagu and N. Gupte, Phys. Rev. E **79**, 066203 (2009).
[20] A. Daitche and T. Tél, Phys. Rev. E **79**, 016210 (2009).
[21] J. H. E. Cartwright, U. Feudel, G. Károlyi, A. P. S. de Moura, O. Piro, and T. Tél, *Dynamics of Finite-Size Particles in Chaotic Fluid Flows* (Springer, Berlin/Heidelberg, 2010), pp. 51–87.
[22] H. Aref *et al.*, Rev. Mod. Phys. **89**, 025007 (2017).
[23] M. Feingold, L. P. Kadano, and O. Piro, J. Stat. Phys. **50**, 529 (1988).
[24] R. S. MacKay, J. Nonlin. Sci. **4**, 329 (1994).
[25] J. H. E. Cartwright, M. Feingold, and O. Piro, Phys. Rev. Lett. **75**, 3669 (1995).
[26] X. Z. Tang and A. H. Boozer, Phys. Fluids **11**, 1418 (1999).
[27] A. Babiano, J. H. E. Cartwright, O. Piro, and A. Provenzale, Phys. Rev. Lett. **84**, 5764 (2000).
[28] S. Das and N. Gupte, Phys. Rev. E **90**, 012906 (2014).
[29] M. R. Maxey and J. J. Riley, Phys. Fluids **26**, 883 (1983).
[30] A. E. Motter, Y. C. Lai, and C. Grebogi, Phys. Rev. E **68**, 056307 (2003).
[31] O. Piro and M. Feingold, Phys. Rev. Lett. **61**, 1799 (1988).
[32] A. Crisanti, M. Falcioni, A. Provenzale, and A. Vulpiani, Phys. Lett. A **150**, 79 (1990).
[33] P. Tanga and A. Provenzale, Physica D **76**, 202 (1994).
[34] A. Babiano, J. H. E. Cartwright, O. Piro, and A. Provenzale, *The Transport of Small Particles by a Fluid* (Springer, Berlin/Heidelberg, 2001), pp. 114–124.
[35] E. E. Michaelides, J. Fluids Eng. **119**, 233 (1997).
[36] T. Dombre, U. Frisch, J. M. Greene, M. Hénon, A. Mehr, and A. M. Soward, J. Fluid Mech. **167**, 353 (1986).
[37] A similar embedding has been studied for the standard map in Refs. [18,19].
[38] J. Bec, L. Biferale, M. Cencini, A. Lanotte, S. Musacchio, and F. Toschi, Phys. Rev. Lett. **98**, 084502 (2007).
[39] I. J. Benczik, Z. Toroczkai, and T. Tél, Phys. Rev. E **67**, 036303 (2003).
[40] R. D. Vilela, T. Tél, A. P. S. de Moura, and C. Grebogi, Phys. Rev. E **75**, 065203 (2007).
[41] J. K. Eaton and J. R. Fessler, Int. J. Multiph. Flow **20**, 169 (1994).
[42] J. R. Angilella, R. D. Vilela, and A. E. Motter, J. Fluid Mech. **744**, 183 (2014).
[43] A. M. Lacasta, J. M. Sancho, A. H. Romero, I. M. Sokolov, and K. Lindenberg, Phys. Rev. E **70**, 051104 (2004).
[44] V. Zaburdaev, M. Schmiedeberg, and H. Stark, Phys. Rev. E **78**, 011119 (2008).
[45] G. M. Zaslavsky, Phys. Rep. **371**, 461 (2002).
[46] E. G. Altmann and H. Kantz, Phys. Rev. E **71**, 056106 (2005).
[47] O. Alus, S. Fishman, and J. D. Meiss, Phys. Rev. E **90**, 062923 (2014).
[48] J. D. Meiss, Chaos **25**, 097602 (2015).
[49] S. Lange, A. Bäcker, and R. Ketzmerick, Europhys. Lett. **116**, 30002 (2016).
[50] R. M. da Silva, M. W. Beims, and C. Manchein, Phys. Rev. E **92**, 022921 (2015).
[51] I. I. Shevchenko, Phys. Rev. E **81**, 066216 (2010).
[52] P. Collins, Z. C. Kramer, B. K. Carpenter, G. S. Ezra, and S. Wiggins, J. Chem. Phys. **141**, 034111 (2014).
[53] A. Sethi and S. Keshavamurthy, Mol. Phys. **110**, 717 (2012).
[54] A. Daitche and T. Tél, Phys. Rev. Lett. **107**, 244501 (2011).
[55] K. Guseva, U. Feudel, and T. Tél, Phys. Rev. E **88**, 042909 (2013).
[56] A. Daitche and T. Tél, New J. Phys. **16**, 073008 (2014).
[57] S. Childress, J. Math. Phys. **11**, 3063 (1970).
[58] H. K. Moffatt, The topology of turbulence, in *New Trends in Turbulence: Nouveaux Aspects*, edited by M. Lesieur, A. M. Yaglom, and F. David, Les Houches-Ecole d'Ete de Physique Theorique (Springer, Berlin/Heidelberg, 2003).
[59] H. K. Moffatt, G. M. Zaslavsky, P. Comte, and M. Tabor, *Topological Aspects of the Dynamics of Fluids and Plasmas*, Nato Science Series E (Springer, Netherlands, 2013).
[60] A. K. Ram, B. Dasgupta, V. Krishnamurthy, and D. Mitra, Phys. Plasmas **21**, 072309 (2014).